

Fast Quantum Nondemolition Readout by Parametric Modulation of Longitudinal Qubit-Oscillator Interaction

Nicolas Didier,^{1,2} Jérôme Bourassa,³ and Alexandre Blais^{2,4}

¹*Department of Physics, McGill University, 3600 rue University, Montreal, Quebec H3A 2T8, Canada*

²*Département de Physique, Université de Sherbrooke, 2500 boulevard de l'Université, Sherbrooke, Québec J1K 2R1, Canada*

³*Cégep de Granby, 235, rue Saint-Jacques, Granby, Québec J2G 9H7, Canada*

⁴*Canadian Institute for Advanced Research, Toronto, Ontario M5G 1Z8, Canada*

(Received 27 April 2015; revised manuscript received 13 July 2015; published 9 November 2015)

We show how to realize fast and high-fidelity quantum nondemolition qubit readout using longitudinal qubit-oscillator interaction. This is accomplished by modulating the longitudinal coupling at the cavity frequency. The qubit-oscillator interaction then acts as a qubit-state dependent drive on the cavity, a situation that is fundamentally different from the standard dispersive case. Single-mode squeezing can be exploited to exponentially increase the signal-to-noise ratio of this readout protocol. We present an implementation of this longitudinal parametric readout in circuit quantum electrodynamics and a possible multiqubit architecture.

DOI: 10.1103/PhysRevLett.115.203601

PACS numbers: 42.50.Dv, 03.65.Ta, 03.67.-a, 42.50.Lc

Introduction.—For quantum information processing, qubit readout must be fast, of high fidelity, and ideally quantum nondemolition (QND). In order to rapidly reuse the measured qubit, fast reset of the measurement pointer states is also needed. Combining these characteristics is essential to meet the stringent requirements of fault-tolerant quantum computation [1]. A common strategy, known as dispersive readout, relies on coupling the qubit to an oscillator acting as the pointer. With the qubit modifying the oscillator frequency in a state-dependent fashion, driving the oscillator displaces its initial vacuum state to qubit-state dependent coherent states. Resolving these pointer states by homodyne detection completes the qubit measurement. This approach is used with superconducting qubits [2–6] and quantum dots [7,8], and is studied in a wide range of systems including donor-based spin qubits [9] and Majorana fermions [10–12]. The same qubit-oscillator interaction is used to measure the oscillator state in cavity QED with Rydberg atoms [13].

In this Letter, we show that parametric modulation of longitudinal qubit-oscillator interaction leads to a faster, very high-fidelity and ideally QND qubit readout with a simple reset mechanism. Moreover, we show how to exponentially improve the signal-to-noise ratio (SNR) of this measurement with the help of a single-mode squeezed input state on the oscillator. Like dispersive readout, this approach is applicable to a wide variety of systems. We start by presenting the performances of longitudinal parametric readout and finally consider as an example an implementation with transmon qubits [14].

While dispersive readout of $\hat{\sigma}_z$ is based on transversal qubit-oscillator coupling, $\hat{H}_x = g_x(\hat{a}^\dagger + \hat{a})\hat{\sigma}_x$, here we propose to use longitudinal interaction, $\hat{H}_z = g_z(\hat{a}^\dagger + \hat{a})\hat{\sigma}_z$. Despite the apparently minimal change we show that, for several reasons, this leads to vastly improved qubit readout.

First, longitudinal coupling leads to an optimal separation of the pointer states. Indeed, \hat{H}_z is simply the generator of displacement of the oscillator field with a qubit-state dependent direction. The resulting evolution from the initial oscillator vacuum state is illustrated in phase space by the full lines of Fig. 1(a). This is to be contrasted to dispersive readout which, as illustrated by the dashed lines, leads to a complex path in phase space and, in particular, to a poor separation of the pointer states at short times (see colored

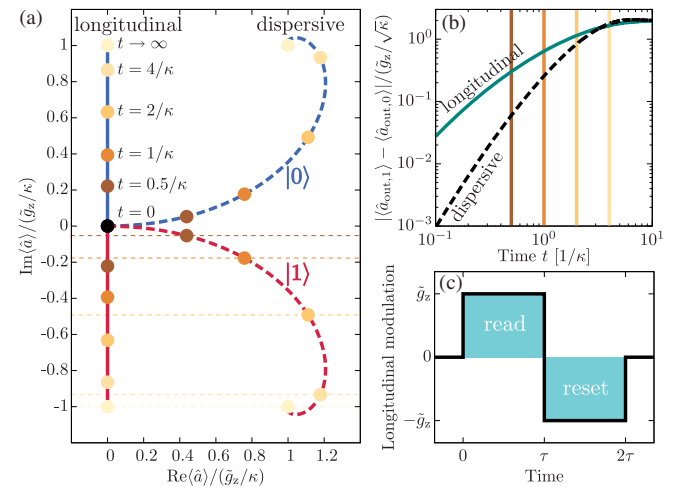


FIG. 1 (color online). (a) Evolution in phase space of the intracavity field \hat{a} for longitudinal (full lines) and dispersive coupling (dashed lines, dispersive shift $\chi = \kappa/2$). Blue and red refer to qubit states. The circles illustrate the position of the pointer states at characteristic times until steady state. (b) Pointer state separation for the cavity output field \hat{a}_{out} as a function of time. Vertical lines correspond to the circles of panel (a). (c) Readout-reset cycle. After a measurement time τ , the sign of the longitudinal modulation amplitude is changed during a time τ to move the pointer state to the origin irrespective of the qubit state.

dots). For this reason, even for identical steady-state separation of the pointers, longitudinal parametric readout is significantly faster than its dispersive counterpart.

A second advantage of the present approach is that it also allows for larger pointer state separations. This is a consequence of the fact that \hat{H}_z commutes with the measured qubit observable, $\hat{\sigma}_z$, resulting in an ideally QND readout. The situation is different for the dispersive case simply because $[\hat{H}_x, \hat{\sigma}_z] \neq 0$. In the dispersive regime, where the qubit-oscillator detuning Δ is large with respect to g_x , this non-QNDness manifests itself with Purcell decay $\gamma_\kappa = (g_x/\Delta)^2\kappa$ [15], where κ is the oscillator damping rate, and with the experimentally observed measurement-induced qubit transitions [16,17]. For these reasons, the oscillator damping rate cannot be made arbitrarily large and the measurement photon number \bar{n} is typically kept well below the critical photon number $n_{\text{crit}} = (\Delta/2g_x)^2$ [2]. In other words, dispersive readout is typically slow (small κ) and limited to poor pointer state separation (small \bar{n}). Because longitudinal coupling is genuinely QND, it does not suffer from these two limitations [18,19].

Longitudinal parametric readout.—Under longitudinal coupling, the qubit-cavity Hamiltonian reads ($\hbar = 1$)

$$\hat{H} = \omega_r \hat{a}^\dagger \hat{a} + \frac{1}{2} \omega_a \hat{\sigma}_z + g_z \hat{\sigma}_z (\hat{a}^\dagger + \hat{a}), \quad (1)$$

where ω_r and ω_a are respectively the cavity and qubit frequencies, while g_z is the longitudinal coupling strength. The realization of multiqubit gates based on this interaction has already been discussed in the context of trapped ions [20–23] and superconducting qubits [18,19,24]. In steady state, Eq. (1) leads to a qubit-state dependent displacement of the cavity field of amplitude $\pm g_z/(\omega_r + i\kappa/2)$. In other words, a static longitudinal interaction is of no consequence for the typical case where $\omega_r \gg g_z, \kappa$.

Here we propose to render this interaction resonant during readout by modulating the coupling at the resonator frequency: $g_z(t) = \tilde{g}_z + \tilde{g}_z \cos(\omega_r t)$. In the interaction picture and neglecting fast-oscillating terms we obtain

$$\tilde{H} = \frac{1}{2} \tilde{g}_z \hat{\sigma}_z (\hat{a}^\dagger + \hat{a}). \quad (2)$$

This now leads to a large qubit-state dependent displacement $\pm \tilde{g}_z/\kappa$. Even with a conservative modulation amplitude $\tilde{g}_z \sim 10\kappa$, the steady-state displacement corresponds to 100 photons and the two qubit states are easily distinguishable by homodyne detection. With this longitudinal coupling, there is no concept of critical photon number and a large photon population is therefore not expected to perturb the qubit. Moreover, as already illustrated in Fig. 1(a), the pointer states take the optimal path in phase space towards their steady-state separation. As shown in Fig. 1(b), this leads to a large pointer state separation at short times.

The consequences of this observation on qubit measurement can be quantified with the SNR. This quantity is

evaluated using $\hat{M}(\tau) = \sqrt{\kappa} \int_0^\tau dt [\hat{a}_{\text{out}}^\dagger(t) + \hat{a}_{\text{out}}(t)]$, the measurement operator for homodyne detection of the output signal \hat{a}_{out} with a measurement time τ . The signal is defined as $|\langle \hat{M} \rangle_1 - \langle \hat{M} \rangle_0|$, where $\{0, 1\}$ refers to the qubit state, while the imprecision noise is $[\langle \hat{M}_{N1}^2(\tau) \rangle + \langle \hat{M}_{N0}^2(\tau) \rangle]^{1/2}$ with $\hat{M}_N = \hat{M} - \langle \hat{M} \rangle$ [25]. Combining these expressions, the SNR for the longitudinal case reads [26]

$$\text{SNR}_z = \sqrt{8} \frac{|\tilde{g}_z|}{\kappa} \sqrt{\kappa\tau} \left[1 - \frac{2}{\kappa\tau} (1 - e^{-\kappa\tau/2}) \right]. \quad (3)$$

This is to be contrasted to SNR_χ for dispersive readout with drive amplitude ϵ and optimal dispersive coupling $\chi = g_x^2/\Delta = \kappa/2$ [25,26,33],

$$\text{SNR}_\chi = \sqrt{8} \frac{|\epsilon|}{\kappa} \sqrt{\kappa\tau} \left[1 - \frac{2}{\kappa\tau} \left(1 - e^{-\kappa\tau/2} \cos \frac{1}{2} \kappa\tau \right) \right]. \quad (4)$$

Both expressions have a similar structure, making very clear the similar role of \tilde{g}_z and ϵ , except for the cosine in Eq. (4) that is a signature of the complex dispersive path in phase space. For short measurement times $\kappa\tau \ll 1$ we find a favorable scaling for longitudinal parametric readout with $\text{SNR}_z \propto \text{SNR}_\chi/\kappa\tau$. This advantage is illustrated in Fig. 2(a)

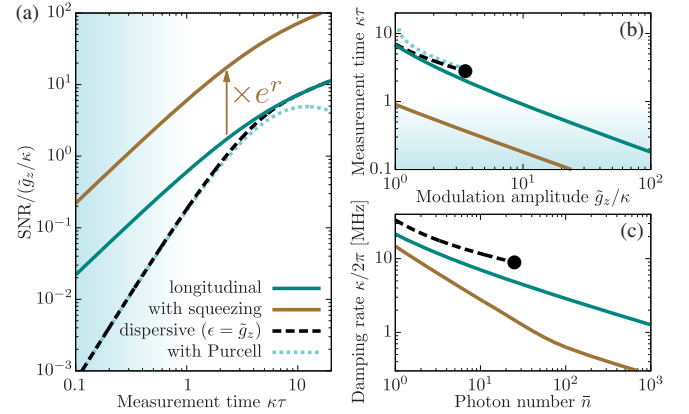


FIG. 2 (color online). (a) SNR in units of \tilde{g}_z/κ as a function of integration time τ . Longitudinal coupling (full green line) is compared to dispersive coupling (dashed black line, $\chi = \kappa/2$) for the same steady-state separation, $|\tilde{g}_z| = |\epsilon|$. The dotted cyan line accounts for Purcell decay in dispersive readout. The full brown line shows the exponential improvement obtained for a single-mode squeezed input state with $e^{2r} = 100$ (20 dB). (b) Measurement time τ required to achieve a fidelity $F = 99.99\%$ versus longitudinal coupling modulation. (c) Cavity damping rate $\kappa/2\pi$ to reach a fidelity of 99.99% in $\tau = 50$ ns versus intracavity photon number $\bar{n} = (\tilde{g}_z/\kappa)^2 = 2(\epsilon/\kappa)^2$. Squeezing (full brown line) helps in further reducing the required photon number or cavity decay rate. The squeeze strength is optimized for each κ , with a maximum set to 20 dB reached close to $\kappa/2\pi = 1$ MHz. In panels (b) and (c), the results for the dispersive readout are stopped at the critical photon number obtained for a drive strength, $\epsilon_{\text{crit}} = \Delta/\sqrt{8}g_x$ for $g_x/\Delta = 1/10$.

showing the SNR versus integration time for longitudinal (full green line) and dispersive without Purcell decay (dashed black line) coupling. Even for equal steady-state separation ($\tilde{g}_z = \epsilon$), this leads to a shorter measurement time for longitudinal coupling. This is made clear in Fig. 2(b), showing the measurement time required to reach a fidelity of 99.99% as a function of \tilde{g}_z/κ (or ϵ/κ for the dispersive case). When taking into account the nonperturbative effects that affect the QNDness of dispersive readout, the advantage of the present approach is made even clearer. This is illustrated by the dotted light-blue lines of Figs. 2(a) and 2(b) corresponding to the dispersive case with Purcell decay. In this more realistic case, longitudinal readout outperforms its counterpart at all times.

Up to now, we have assumed equal pointer state separation for the two readouts. As already mentioned, dispersive readout is, however, limited to measurement photon numbers well below n_{crit} . This is taken into account in Figs. 2(b) and 2(c) by stopping the dispersive curves at n_{crit} (black circle) assuming the typical value, $g_x/\Delta = 1/10$. Panel (b) makes it very clear that only longitudinal readout allows for measurement times $< 1/\kappa$. This is, moreover, achieved for reasonable modulation amplitudes with respect to the cavity linewidth. As a further illustration, panel (c) shows the cavity damping rate versus photon number required to reach a fidelity of 99.99% in $\tau = 50$ ns. Note that the dotted blue line corresponding to the dispersive case with Purcell decay is absent from this plot. In other words, with dispersive readout it appears impossible to achieve the above target fidelity and measurement time in the very wide range of parameters of Fig. 2(c). On the other hand, this is achievable with longitudinal readout with quite moderate values of κ and \bar{n} . Further speedups are possible with pulse shaping [6,34] and machine learning [35]. Because the pointer state separation is optimal even at short times, the latter approach should be particularly efficient.

To allow for rapid reuse of the qubit, the cavity should be returned to its ground state ideally in a time $\ll 1/\kappa$ after readout. A pulse sequence achieving this for dispersive readout has been proposed but is imperfect because of qubit-induced nonlinearity deriving from \hat{H}_x [34]. As illustrated in Fig. 1(c), in the present approach cavity reset is simply realized by inverting the phase of the modulation. Since \hat{H}_z does not lead to qubit-induced nonlinearity, this reset is ideal. In practice, reset can also be shorter than the integration time. It is also interesting to point out that longitudinal parametric readout saturates the inequality $\Gamma_{\phi m} \geq \Gamma_{\text{meas}}$ linking the measurement-induced dephasing rate $\Gamma_{\phi m}$ to the measurement rate Γ_{meas} and is therefore quantum limited [26].

Single-mode squeezing.—Another striking feature of this new readout is that its SNR can be exponentially improved by a single-mode squeezed input state on the cavity. For this it suffices to chose the squeeze axis to be orthogonal to

the qubit-state dependent displacement generated by $g_z(t)$. In Fig. 1(a), this corresponds to squeezing along the vertical axis. With this choice, and since the squeeze angle is unchanged under evolution with \hat{H}_z , the imprecision noise is exponentially reduced and the signal-to-noise ratio simply becomes $e^r \text{SNR}_z$, with r the squeeze parameter [26]. This exponential enhancement is apparent from the full brown line in Fig. 2(a) and in the corresponding reduction of the measurement time in Fig. 2(b). Note that by taking $\tilde{g}_z = 0$, the cavity field can be squeezed prior to measurement without negatively affecting the qubit.

This exponential improvement is in stark contrast to standard dispersive readout where single-mode squeezing can lead to an increase of the measurement time [25,36]. Indeed, under dispersive coupling, the squeeze angle undergoes a qubit-state dependent rotation. As a result, both the squeezed and the antisqueezed quadrature contributes to the imprecision noise. We note that the situation can be different in the presence of two-mode squeezing [36] where an exponential increase in SNR can be recovered by engineering the dispersive coupling of the qubit to two cavities [25].

Circuit QED implementation.—While this approach is very general, we now turn to a possible realization in circuit QED [2]. Longitudinal coupling of a flux or transmon qubit to a LC oscillator has already been discussed in Refs. [18,19]. There, longitudinal coupling results from the mutual inductance between a flux-tunable qubit and the oscillator. As another example, we follow the general approach developed in Ref. [37] and focus on a transmon qubit [14] phase biased by the oscillator. Figure 3(a)

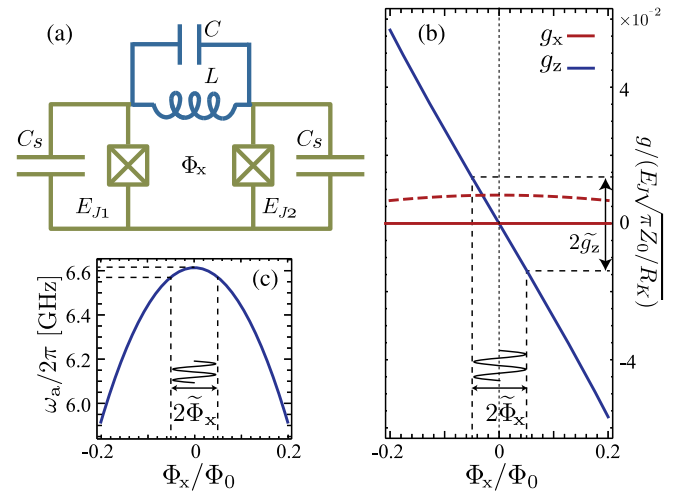


FIG. 3 (color online). (a) Circuit QED implementation of longitudinal coupling with a transmon qubit of Josephson energies $E_{J1} = E_J(1+d)/2$, $E_{J2} = E_J(1-d)/2$ with $d \in [0, 1]$. (b) g_z and g_x versus flux. Around $\Phi_x = 0$, g_z depends linearly on flux. Spurious transverse coupling g_x results from qubit asymmetry. The full (dashed) lines correspond to Eqs. (5) and (6) with $d = 0$ ($d = 0.02$). (c) Transmon frequency versus flux for $E_J/h = 20$ GHz, $E_J/E_C = 67$, and $d = 0.02$.

schematically represents a lumped version of this circuit. In practice, the inductor can be replaced by a junction array [38], both to increase the coupling and to reduce the qubit's flux-bias loop size. An in-depth analysis of an alternative realization based on a transmission-line resonator can be found in Ref. [26].

The Hamiltonian of the circuit of Fig. 3(a) is similar to that of a flux-tunable transmon, but where the external flux Φ_x is replaced by $\Phi_x + \delta$ with δ the phase drop at the oscillator [39]. Taking the junction capacitances to be equal and assuming for simplicity that $Z_0/R_K \ll 1$ with $Z_0 = \sqrt{L/C}$ and R_K the resistance quantum, this Hamiltonian can be expressed as $\hat{H} = \hat{H}_r + \hat{H}_q + \hat{H}_{qr}$. In this expression, $\hat{H}_r = \omega_r \hat{a}^\dagger \hat{a}$ is the oscillator Hamiltonian and $\hat{H}_q = \omega_a \hat{\sigma}_z / 2$ is the Hamiltonian of a flux-tunable transmon written here in its two-level approximation [14]. The qubit-oscillator interaction takes the form $\hat{H}_{qr} = g_x (\hat{a}^\dagger + \hat{a}) \hat{\sigma}_x + g_z (\hat{a}^\dagger + \hat{a}) \hat{\sigma}_z$ with [26]

$$g_z = -\frac{E_J}{2} \left(\frac{2E_C}{E_J} \right)^{1/2} \sqrt{\frac{\pi Z_0}{R_K}} \sin\left(\frac{\pi \Phi_x}{\Phi_0}\right), \quad (5)$$

$$g_x = dE_J \left(\frac{2E_C}{E_J} \right)^{1/4} \sqrt{\frac{\pi Z_0}{R_K}} \cos\left(\frac{\pi \Phi_x}{\Phi_0}\right), \quad (6)$$

where E_J is the mean Josephson energy, d the Josephson energy asymmetry, and E_C the qubit's charging energy. Expressions for these quantities in terms of the elementary circuit parameters are given in Ref. [26]. As desired, the transverse coupling g_x vanishes exactly for $d = 0$, leaving only longitudinal coupling g_z . Thanks to the phase bias, rather than inductive coupling, g_z can be made large [37]. For example, with the realistic values $E_J/h = 20$ GHz, $E_J/E_C = 67$, and $Z_0 = 50 \Omega$ we find $g_z/2\pi \approx 135$ MHz $\times \sin(\pi \Phi_x / \Phi_0)$. The flux dependence of both g_z (blue line) and g_x with $d = 0$ (full red line) and $d = 0.02$ (dashed red line) are illustrated in Fig. 3(b). Modulating the flux by $0.05 \Phi_0$ around $\Phi_x = 0$, we find $\bar{g}_z = 0$ and $\tilde{g}_z/2\pi \sim 21$ MHz. This is accompanied by a small change of the qubit frequency of ~ 40 MHz; see Fig. 3(c). Importantly, this does not affect the SNR [26].

Tolerance to imperfections.—A finite g_x is present for $d \neq 0$. This is illustrated in Fig. 3(b) where for a realistic value of $d = 0.02$ [40] and the above parameters we find $g_x/2\pi \approx 13$ MHz $\times \cos(\pi \Phi_x / \Phi_0)$. The effect of this unwanted coupling can be mitigated by working at large qubit-resonator detuning Δ where the resulting dispersive interaction $\chi = g_x^2/\Delta$ can be made very small. For example, the above numbers correspond to a detuning of $\Delta/2\pi = 3$ GHz where $\chi/2\pi \sim 5.6$ kHz. It is important to emphasize that, contrary to dispersive readout, the longitudinal approach is not negatively affected by a large detuning.

When considering higher-order terms in Z_0/R_K , the Hamiltonian of the circuit of Fig. 3(a) contains a dispersive-like interaction $\chi_z \hat{a}^\dagger \hat{a} \hat{\sigma}_z$ even at $d = 0$. For the parameters already used above, we find $\chi_z/2\pi \sim 5.3$ MHz, a value that is not made smaller by detuning the qubit from the resonator. However, since it is not derived from a transverse coupling, χ_z is not linked to any Purcell decay. Moreover, it does not affect SNR_z at small measurement times [26].

In the absence of measurement, $\bar{g}_z = \tilde{g}_z = 0$ and the qubit is, moreover, parked at its flux sweet spot. Dephasing due to photon shot noise or to low-frequency flux noise is therefore expected to be minimal. Because of the longitudinal coupling, another potential source of dephasing is flux noise at the resonator frequency which will mimic qubit measurement. However, given that the spectral density of flux noise is proportional to $1/f$ even at high frequency [17], this contribution is negligible [26].

Multiqubit architecture.—A possible multiqubit architecture consists of qubits longitudinally coupled to a readout resonator (of annihilation operator \hat{a}_z) and transversally coupled to a high- Q bus resonator (\hat{a}_x). The Hamiltonian describing this system is

$$\begin{aligned} \hat{H} = & \omega_{rz} \hat{a}_z^\dagger \hat{a}_z + \omega_{rx} \hat{a}_x^\dagger \hat{a}_x + \sum_j \frac{1}{2} \omega_{aj} \hat{\sigma}_{zj} \\ & + \sum_j g_{zj} \hat{\sigma}_{zj} (\hat{a}_z^\dagger + \hat{a}_z) + \sum_j g_{xj} \hat{\sigma}_{xj} (\hat{a}_x^\dagger + \hat{a}_x). \end{aligned} \quad (7)$$

Readout can be realized using longitudinal coupling while logical operations can be done via the bus resonator. An alternative architecture taking advantage of longitudinal coupling is discussed at length in Ref. [19]. Here, taking $g_{zj}(t) = \bar{g}_z + \tilde{g}_z \cos(\omega_r t + \varphi_j)$, the longitudinal coupling becomes, in the interaction picture and neglecting fast-oscillating terms,

$$\tilde{H}_z = \left(\frac{1}{2} \tilde{g}_z \sum_j \hat{\sigma}_{zj} e^{-i\varphi_j} \right) \hat{a}_z + \text{H.c.} \quad (8)$$

This effective resonator drive displaces the field to multiqubit-state dependent coherent states. For two qubits, taking $\varphi_j = j\pi/2$ leads to the four pointer states separated by 90° from each other or, in other words, to optimal separation even at short times. Other choices of phase lead to overlapping pointer states corresponding to different multiqubit states. Examples are $\varphi_j = 0$ for which $|01\rangle$ and $|10\rangle$ are indistinguishable, and $\varphi_j = j\pi$ where these states are replaced by $|00\rangle$ and $|11\rangle$. This can be exploited to create entanglement by measurement [41]. As a final example, with three qubits the GHZ state is obtained with $\varphi_j = j2\pi/3$ [26].

Conclusion.—We have proposed a new approach for qubit readout based on the modulation of longitudinal qubit-oscillator coupling. This new mechanism has several

advantages over the standard dispersive readout: optimal pointer state separation, purely QND (thereby avoiding Purcell decay and allowing large pointer state separation), rapid reset, and exponential improvement of the SNR using single-mode squeezing. This is applicable to a wide variety of physical systems and we have used circuit QED with transmon qubits as a concrete example.

We thank A. Clerk for useful discussions. This work was supported by the Army Research Office under Grant No. W911NF-14-1-0078, INTRIQU, and NSERC.

-
- [1] R. Raussendorf and J. Harrington, *Phys. Rev. Lett.* **98**, 190504 (2007).
- [2] A. Blais, R.-S. Huang, A. Wallraff, S. M. Girvin, and R. J. Schoelkopf, *Phys. Rev. A* **69**, 062320 (2004).
- [3] R. Vijay, D. H. Slichter, and I. Siddiqi, *Phys. Rev. Lett.* **106**, 110502 (2011).
- [4] R. Vijay, C. Macklin, D. H. Slichter, S. J. Weber, K. W. Murch, R. Naik, A. N. Korotkov, and I. Siddiqi, *Nature (London)* **490**, 77 (2012).
- [5] M. Hatridge, S. Shankar, M. Mirrahimi, F. Schackert, K. Geerlings, T. Brecht, K. M. Sliwa, B. Abdo, L. Frunzio, S. M. Girvin, R. J. Schoelkopf, and M. H. Devoret, *Science* **339**, 178 (2013).
- [6] E. Jeffrey, D. Sank, J. Y. Mutus, T. C. White, J. Kelly, R. Barends, Y. Chen, Z. Chen, B. Chiaro, A. Dunsworth, A. Megrant, P. J. J. O'Malley, C. Neill, P. Roushan, A. Vainsencher, J. Wenner, A. N. Cleland, and J. M. Martinis, *Phys. Rev. Lett.* **112**, 190504 (2014).
- [7] T. Frey, P. J. Leek, M. Beck, A. Blais, T. Ihn, K. Ensslin, and A. Wallraff, *Phys. Rev. Lett.* **108**, 046807 (2012).
- [8] K. D. Petersson, L. W. McFaul, M. D. Schroer, M. Jung, J. M. Taylor, A. A. Houck, and J. R. Petta, *Nature (London)* **490**, 380 (2012).
- [9] G. Tosi, F. A. Mohiyaddin, H. Huebl, and A. Morello, *AIP Adv.* **4**, 087122 (2014).
- [10] F. Hassler, A. R. Akhmerov, and C. W. J. Beenakker, *New J. Phys.* **13**, 095004 (2011).
- [11] C. Müller, J. Bourassa, and A. Blais, *Phys. Rev. B* **88**, 235401 (2013).
- [12] E. Ginossar and E. Grosfeld, *Nat. Commun.* **5**, 4772 (2014).
- [13] S. Haroche and J.-M. Raimond, *Exploring the Quantum: Atoms, Cavities, and Photons* (Oxford University Press, Oxford, 2006).
- [14] J. Koch, T. M. Yu, J. Gambetta, A. A. Houck, D. I. Schuster, J. Majer, A. Blais, M. H. Devoret, S. M. Girvin, and R. J. Schoelkopf, *Phys. Rev. A* **76**, 042319 (2007).
- [15] A. A. Houck, J. A. Schreier, B. R. Johnson, J. M. Chow, J. Koch, J. M. Gambetta, D. I. Schuster, L. Frunzio, M. H. Devoret, S. M. Girvin, and R. J. Schoelkopf, *Phys. Rev. Lett.* **101**, 080502 (2008).
- [16] M. Boissonneault, J. M. Gambetta, and A. Blais, *Phys. Rev. A* **79**, 013819 (2009).
- [17] D. H. Slichter, R. Vijay, S. J. Weber, S. Boutin, M. Boissonneault, J. M. Gambetta, A. Blais, and I. Siddiqi, *Phys. Rev. Lett.* **109**, 153601 (2012).
- [18] A. J. Kerman, *New J. Phys.* **15**, 123011 (2013).
- [19] P.-M. Billangeon, J. S. Tsai, and Y. Nakamura, *Phys. Rev. B* **91**, 094517 (2015).
- [20] G. Milburn, S. Schneider, and D. James, *Fortschr. Phys.* **48**, 801 (2000).
- [21] A. Sørensen and K. Mølmer, *Phys. Rev. A* **62**, 022311 (2000).
- [22] J. J. Garcia-Ripoll, P. Zoller, and J. I. Cirac, *Phys. Rev. Lett.* **91**, 157901 (2003).
- [23] D. Leibfried, B. DeMarco, V. Meyer, D. Lucas, M. Barrett, J. Britton, W. M. Itano, B. Jelenkovic, C. Langer, T. Rosenband, and D. J. Wineland, *Nature (London)* **422**, 412 (2003).
- [24] A. Blais, J. Gambetta, A. Wallraff, D. I. Schuster, S. M. Girvin, M. H. Devoret, and R. J. Schoelkopf, *Phys. Rev. A* **75**, 032329 (2007).
- [25] N. Didier, A. Kamal, W. D. Oliver, A. Blais, and A. A. Clerk, *Phys. Rev. Lett.* **115**, 093604 (2015).
- [26] See Supplemental Material at <http://link.aps.org/supplemental/10.1103/PhysRevLett.115.203601>, which includes Refs. [27–32], for the derivation of the signal-to-noise ratios, detailed calculations for longitudinal coupling with a coplanar resonator and details of the multiqubit architecture.
- [27] C. Gardiner and P. Zoller, *Quantum Noise*, 3rd ed. (Springer, New York, 2004).
- [28] A. Clerk, M. Devoret, S. Girvin, F. Marquardt, and R. Schoelkopf, *Rev. Mod. Phys.* **82**, 1155 (2010).
- [29] M. H. Devoret, in *Les Houches, Session LXIII, 1995*, edited by S. Reynaud, E. Giacobino, and J. Zinn-Justin (Elsevier Science, Amsterdam, 1997), p. 351.
- [30] J. Bourassa, F. Beaudoin, J. M. Gambetta, and A. Blais, *Phys. Rev. A* **86**, 013814 (2012).
- [31] C. Eichler and A. Wallraff, *EPJ Quantum Technology* **1**, 2 (2014).
- [32] N. A. Masluk, I. M. Pop, A. Kamal, Z. K. Mineev, and M. H. Devoret, *Phys. Rev. Lett.* **109**, 137002 (2012).
- [33] J. Gambetta, A. Blais, M. Boissonneault, A. A. Houck, D. I. Schuster, and S. M. Girvin, *Phys. Rev. A* **77**, 012112 (2008).
- [34] D. T. McClure, H. Paik, L. S. Bishop, M. Steffen, J. M. Chow, and J. M. Gambetta, *arXiv:1503.01456*.
- [35] E. Magesan, J. M. Gambetta, A. D. Córcoles, and J. M. Chow, *Phys. Rev. Lett.* **114**, 200501 (2015).
- [36] S. Barzanjeh, D. P. DiVincenzo, and B. M. Terhal, *Phys. Rev. B* **90**, 134515 (2014).
- [37] J. Bourassa, J. M. Gambetta, A. A. Abdumalikov, O. Astafiev, Y. Nakamura, and A. Blais, *Phys. Rev. A* **80**, 032109 (2009).
- [38] V. E. Manucharyan, J. Koch, L. I. Glazman, and M. H. Devoret, *Science* **326**, 113 (2009).
- [39] D. Vion, A. Aassime, A. Cottet, P. Joyez, H. Pothier, C. Urbina, D. Esteve, and M. Devoret, *Science* **296**, 886 (2002).
- [40] J. M. Fink, R. Bianchetti, M. Baur, M. Göppl, L. Steffen, S. Filipp, P. J. Leek, A. Blais, and A. Wallraff, *Phys. Rev. Lett.* **103**, 083601 (2009).
- [41] K. Lalumière, J. M. Gambetta, and A. Blais, *Phys. Rev. A* **81**, 040301 (2010).